Transducer-Shadow Effects on Turbulence Spectra Measured by Sonic Anemometers

JOHN C. WYNGAARD

National Center for Atmospheric Research, Boulder, CO 80307*

SHI-FENG ZHANG

Department of Atmospheric Sciences, University of Washington, Seattle, WA 98105

(Manuscript received 29 December 1984, in final form 8 April 1985)

ABSTRACT

We show that the horizontal turbulent velocity components measured by the common sonic anemometer array can suffer attenuation and crosstalk as a result of the flow blockage caused by the acoustic transducer assemblies. Using an analytical model of this "transducer-shadow effect", flow-blockage data from test arrays, and a simple linear model of the fluctuating response, we show the nature of the distortion in the measured velocity spectra. We suggest that rather than correct for the shadow effect, which can be quite significant for horizontal velocity spectra and stress cospectra, it would be preferable to minimize it through design. There is encouraging evidence that the Kaijo–Denki transducer design produces much less shadow effect than the conventional (right circular cylinder) shape.

1. Introduction

Kaimal (1979) refers to the sonic anemometer as the "instrument of choice" among boundary layer physicists seeking fair-weather observations of atmospheric turbulence. Summarizing the reasons for this favored position, he points out that it has no moving parts to come into dynamic equilibrium with the flow, so its frequency response is limited only through the spatial filtering imposed by line averaging along the path. It responds linearly to wind velocity and is relatively free of contamination from other velocity components or temperature. Finally, he points out that as an absolute instrument, its calibration is established by its design parameters.

Although its operating principle is simple, a sonic anemometer is a complex instrument and understanding its response can be quite challenging. Kaimal (1979) surveys the progress that has been made in analyzing the effects of finite path length and path separation (Kaimal *et al.*, 1968; Horst, 1973), sound-speed fluctuations (Friehe, 1976), leveling errors (Kaimal and Haugen, 1969), and transducer shadows. All but the last seem well understood.

The shadow effect refers to the velocity deficit in the transducer wakes along the acoustic paths. It seems to have been discussed first by Kaimal (1979), who presented some measurements of the resulting path-averaged velocity errors in a simple array. In his review paper, Wyngaard (1981a) pointed out that the shadow effect could be important in short-path arrays, and Kaimal and Gaynor (1983) show how it is being accounted for in the sonic anemometers at the Boulder Atmospheric Observatory. Hanafusa *et al.* (1982) and Coppin and Taylor (1983) discuss new, improved sonic anemometers but show that they also suffer from transducer-shadow effects.

Mestayer (1982) suggested that transducer-shadow effects could be the source of the spectral attenuation that he detected in sonic anemometer data. Hanafusa *et al.* (1982), on the other hand, on the basis of some brief field trials with two units mounted close together but with a 45-degree difference in orientation, found "no remarkable difference" in their output statistics (mean wind speed and direction and horizontal velocity variance). They concluded that "the difference causes no trouble in the use of those instruments in the field." However, Coppin and Taylor (1983) were clearly concerned about shadow effects. They wrote that "deficiencies in horizontal directional response appear to be a major limitation in the field use of sonic anemometers."

While there has been recent concern about the effects of transducer shadows on turbulence statistics measured by sonic anemometers, there has not been a definitive assessment of these effects. Unfortunately, it is difficult to study this problem experimentally, because the flow distortion in typical arrays can also influence the turbulence statistics (Wyngaard, 1981b), and it is not clear if the two sets of effects can be isolated.

As a first step toward this assessment, therefore, we present a theoretical analysis of transducer-shadow ef-

* The National Center for Atmospheric Research is sponsored by the National Science Foundation.

fects on turbulence spectra measured by the most common sonic array.

2. The transducer-shadow effect

Figures 1 and 2 (from Kaimal, 1979) show commercial three-axis sonic anemometer arrays. The unit shown in Fig. 1 is an EGG Model 198-3 used in the 1973 Minnesota experiments (Kaimal *et al.*, 1976), while the unit in Fig. 2 is a Ball Brothers Model 125-197, 198 used at the Boulder Atmospheric Observatory. Each axis has two acoustic paths so that the transit time difference for sound pulses emitted from each end yields the path-averaged value of the wind velocity component in the path direction. The horizontal velocity components are obtained from the pair of horizontal axes, and the vertical axis provides the vertical velocity.

Figure 3 shows the field and commercial model of the short-path (10 cm) array developed by Coppin and Taylor (1983). It has the same basic geometry as the units in Figs. 1 and 2. However, this design uses only one transducer, serving alternately as a transmitter and a receiver, at each end of an axis. Figure 4 shows a Kaijo–Denki unit (Hanafusa *et al.*, 1982) of similar geometry.

As Figs. 1–4 reveal, in these arrays the scale of the transducers and their mounts is not small compared with the path length. Thus, one expects that the flow blockage near the path ends could cause this path-av-

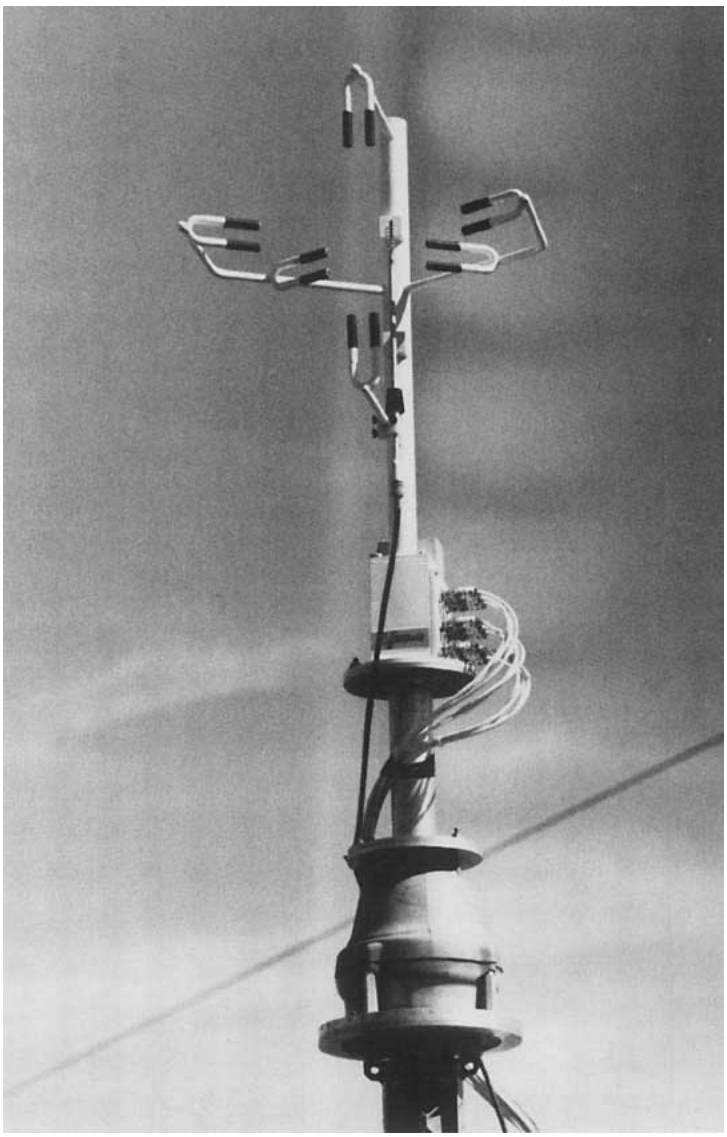

FIG. 1. The three-component sonic array used in the 1973 Minnesota experiments. Photo courtesy J. C. Kaimal.

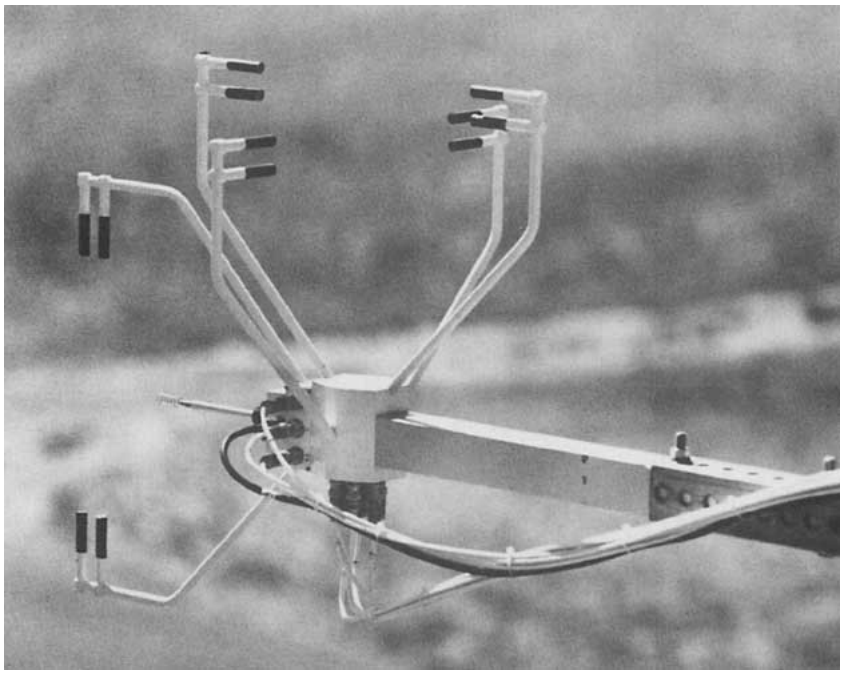

FIG. 2. The three-component sonic array used at the Boulder Atmospheric Observatory. Photo courtesy J. C. Kaimal.

eraged wind velocity component to be somewhat less than its value in the free stream.

Kaimal (1979) demonstrated this transducer-shadow effect through wind tunnel and atmospheric tests. We present his results in Fig. 5, which shows the axial velocity attenuation in a single-axis unit as a function of the inclination θ of the flow vector to the acoustic path. The attenuation is greatest when the flow is along the path, decreases as θ increases, and also decreases as L/d (path length/transducer diameter) increases.

Figure 6 introduces velocity attenuation data at $L/d = 10$ measured in single-axis test arrays by Hanafusa *et al.* (1982) and Coppin and Taylor (1983). While the three sets of results are qualitatively similar, there are substantial differences; in particular, the Hanafusa *et al.* results essentially indicate no attenuation for flow

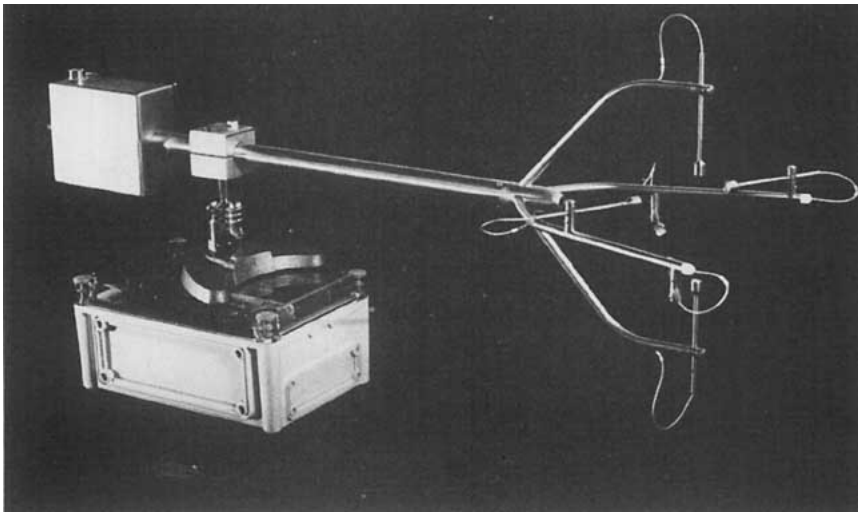

FIG. 3. The Coppin–Taylor sonic anemometer.

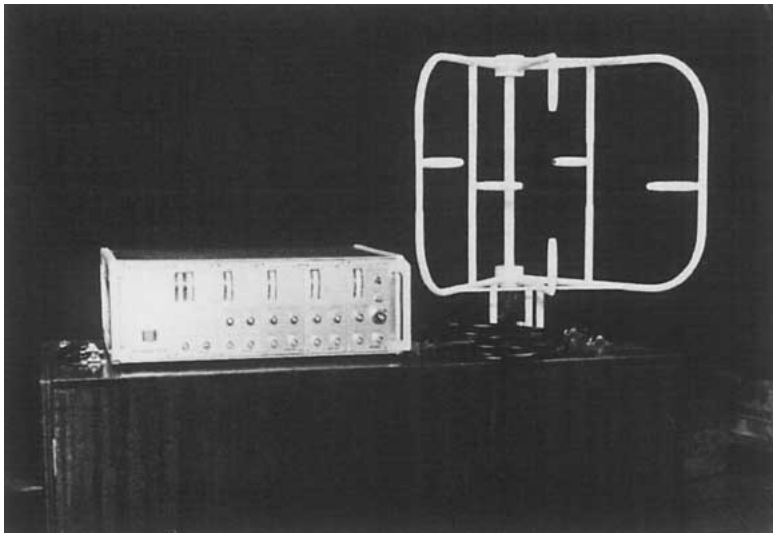

FIG. 4. The Kaijo–Denki sonic anemometer.

angles greater than about 30 degrees, while the Kaimal and Coppin–Taylor tests show significant attenuation until 60–70 degrees. Figure 6 also includes a response curve for the field and commercial model of the Coppin–Taylor anemometer. This curve was provided by Dr. Coppin, who indicated that the improvement in response is due to transducer redesign.

The differences in directional response shown in Fig. 6 are evidently due to differences in transducer geometry. Both the Kaimal (1979) and Coppin–Taylor (1983) tests used transducers in the shape of a right circular cylinder (Figs. 1–3). Hanafusa *et al.* used a specially shaped Kaijo–Denki transducer (Fig. 4) designed to minimize the shadow effect (Mitsuta, 1974); Fig. 6 shows that its response is indeed much improved. The smaller difference between the Coppin–Taylor (1983) and Kaimal (1979) results could be due to their design differences. The Kaimal test array had two

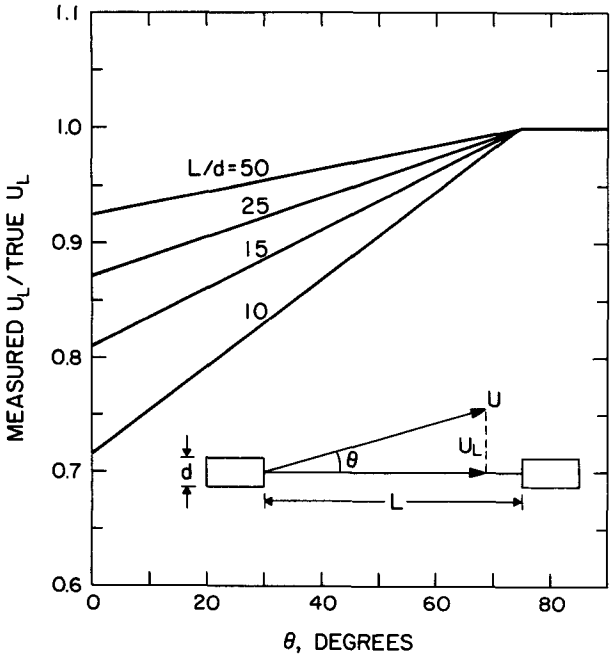

FIG. 5. Kaimal's (1979) curves on axial velocity attenuation in an array with BAO-type transducers.

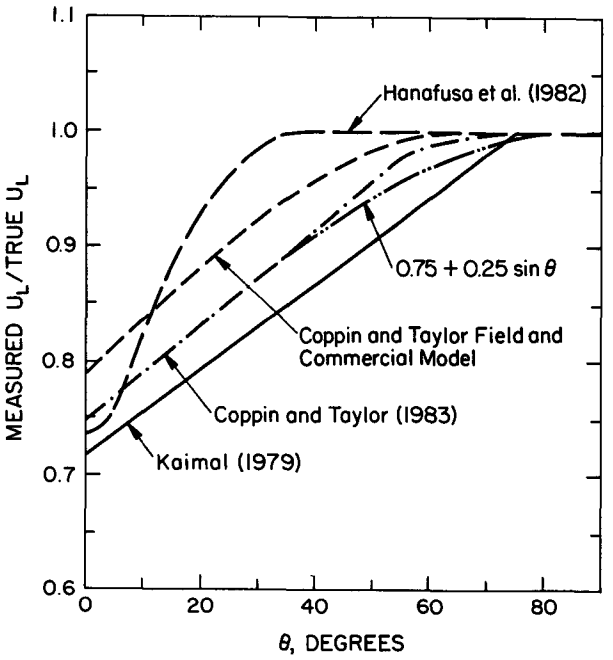

FIG. 6. Axial velocity attenuation at $L/d = 10$, contrasting the behavior of Kaijo–Denki-type and BAO-type transducers.

acoustic paths, one slightly above the other; hence, there were a pair of transducers at each end, as in the arrays of Figs. 1 and 2. The Coppin–Taylor test array had coincident paths, with only one transducer at each end, as in their field and commercial model shown in Fig. 3.

The dependence of the velocity error on L/d indicated by Kaimal's data in Fig. 5 seems plausible physically. One can easily show that if, for fixed flow angle θ and geometrically similar transducers, the axial length of the transducer wake scales with transducer diameter d, then the axial velocity error averaged over the path length L increases linearly with d/L. Figure 7, a plot of the velocity attenuation at $\theta = 0$ versus d/L, shows that this is a reasonable approximation to both the Kaimal and Hanafusa *et al.* test data. Coppin and Taylor showed results for only one d/L value.

Figures 6 and 7 suggest that the dependence of the velocity attenuation on inclination angle θ is more sensitive to the design of the transducer than is its dependence on L/d. We will present calculations for two varieties of transducers: right circular cylinders, used in the arrays of Figs. 1–3, which we will call BAO type; and streamlined transducers (Fig. 4), which we will call Kaijo–Denki type. In order to make our analytical calculations tractable, we will use simple parameterizations of their directional response:

$$U_L^m/U_L = C + (1 - C)\sin\theta \quad \text{(BAO-type)}, \tag{1a}$$

$$U_L^m/U_L = 1 - (1 - C)e^{-a\sin^2\theta} \quad \text{(Kaijo–Denki-type)}. \tag{1b}$$

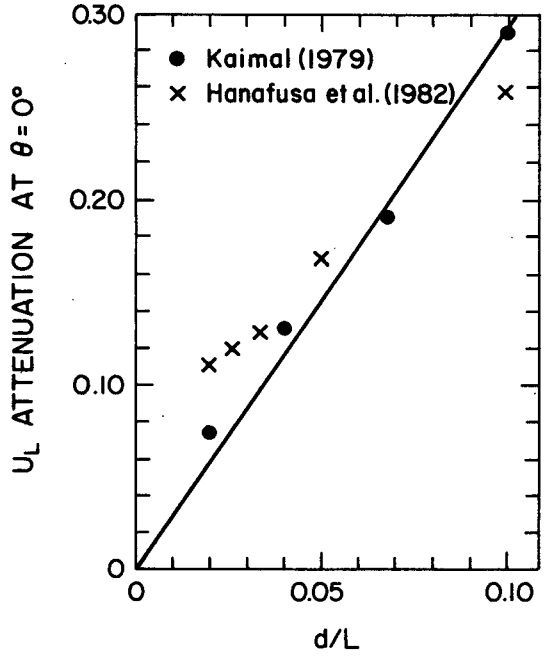

FIG. 7. Axial velocity attenuation at $\theta = 0°$.

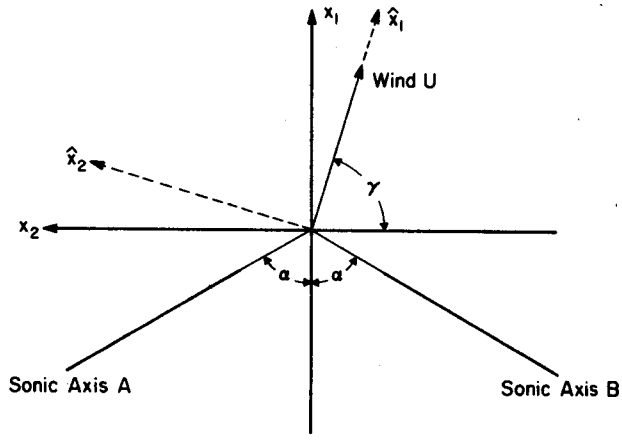

FIG. 8. Geometry of the array used to measure horizontal velocity components.

Here the superscript m means measured value. In each case C is the response at $\theta = 0$. Figure 6 shows that (1a) with $C = 0.75$ is a fairly good fit to the Coppin–Taylor (1983) data; a slightly smaller C would fit the Kaimal data. Equation (1b), with $C = 0.74$ and $a = 11.5$, fits the Hanafusa *et al.* data very well.

3. Effects on velocity spectra

Figure 8 shows the geometry of the horizontal axes of the arrays in Figs. 1–4. Let the two sonic axes, denoted with subscripts A and B, be located symmetrically with respect to the x_1 axis, and let the angle between these axes be 2α. Let the angle between the wind vector and the x_2 axis be γ. Since each sonic axis measures the projection of the wind on its path vector, in the absence of measurement error the outputs would be

$$U_A = U_1\cos\alpha - U_2\sin\alpha, \tag{2}$$

$$U_B = U_1\cos\alpha + U_2\sin\alpha. \tag{3}$$

Thus, we would recover the wind components from

$$U_1 = (U_A + U_B)/(2\cos\alpha), \tag{4}$$

$$U_2 = (U_B - U_A)/(2\sin\alpha). \tag{5}$$

The measured velocity components are subject to the transducer-shadow effects, which we can now incorporate through (1).

a. BAO-type transducers

We consider first an array fitted with BAO-type transducers; that is, ones of right circular cylinder shape, as in the arrays of Figs. 1–3. Using (1a), we write the actual response of the A and B axes as

$$U_A^m = U_A[C + (1 - C)\sin\theta_A] = U_A f_A, \tag{6}$$

$$U_B^m = U_B[C + (1 - C)\sin\theta_B] = U_B f_B. \tag{7}$$

Then from (2) through (7) and the geometry of Fig. 8 we have

$$U_1^m = U_1\left(\frac{f_A + f_B}{2}\right) + U_2 \tan\alpha\left(\frac{f_B - f_A}{2}\right), \quad (8)$$

$$U_2^m = U_1 \cot\alpha\left(\frac{f_B - f_A}{2}\right) + U_2\left(\frac{f_A + f_B}{2}\right), \quad (9)$$

where the shadow functions can be written as

$$\left(\frac{f_A + f_B}{2}\right) = C + (1 - C)\sin\gamma \sin\alpha, \quad (10)$$

$$\left(\frac{f_B - f_A}{2}\right) = (1 - C)\cos\gamma \cos\alpha. \quad (11)$$

In the absence of shadow effects $f_A = f_B = 1$, and (8) and (9) yield $U_1^m = U_1$, $U_2^m = U_2$. With shadow effects, however, we see that the measured horizontal velocity components suffer attenuation and crosstalk (mixing of the two components).

We can write immediately the expression for vertical velocity measured with BAO-type transducers:

$$U_3^m = U_3[C + (1 - C)\sin\theta]. \quad (12)$$

Here θ is the angle between the wind vector and the vertical axis.

Having our basic results (8), (9), and (12), we can now examine transducer-shadow effects on turbulence spectra. We will begin with the horizontal velocity components, for which we will do two calculations. The first uses coordinates aligned with the sonic array, and the second uses the more conventional mean-wind coordinates. Finally, we will briefly discuss the vertical velocity spectrum and stress cospectra.

1) Horizontal velocity spectra in anemometer coordinates

We use coordinates aligned with the axes of symmetry of the sonic anemometer, as shown in Fig. 8. To reveal the effects on turbulence, we begin by decomposing the velocity field into mean and fluctuating components,

$$U_i = \tilde{U}_i + u_i, \quad i = 1, 2, 3, \quad (13)$$

with the lower case denoting the fluctuations. We assume that the rms velocity fluctuations are small compared to the mean, so that we can derive a linearized pair of equations for the turbulent components. After some algebra, (8) and (9) yield

$$u_1^m = c_1 u_1 + c_2 u_2, \quad (14)$$

$$u_2^m = d_1 u_1 + d_2 u_2. \quad (15)$$

Here the coefficients are

$$c_1 = C + (1 - C)\sin\alpha(1 + 2\cos^2\gamma)\sin\gamma, \quad (16)$$

$$c_2 = (1 - C)\sin\alpha \cos\gamma(1 + 2\sin^2\gamma), \quad (17)$$

$$d_1 = 2(1 - C)\cos\alpha \cot 2\alpha \cos^3\gamma, \quad (18)$$

$$d_2 = C - 2(1 - C)\cos\alpha \cot 2\alpha \sin^3\gamma, \quad (19)$$

where γ is the angle of the mean wind vector; i.e.,

$$\tan\gamma = -\tilde{U}_1/\tilde{U}_2. \quad (20)$$

The linear equations (14) and (15) express the attenuation and crosstalk of horizontal turbulent velocity components, referred to the symmetry axes of the sonic array (Fig. 8). They yield simple expressions for the measured spectra:

$$\Phi_1^m = c_1^2\Phi_1 + c_2^2\Phi_2 + 2c_1c_2\mathrm{Co}_{12}, \quad (21)$$

$$\Phi_2^m = d_1^2\Phi_1 + d_2^2\Phi_2 + 2d_1d_2\mathrm{Co}_{12}. \quad (22)$$

Here Φ_1 is the spectrum of u_i.

Let us examine Co_{12}. It is simplest to do this by expressing u_1 and u_2 in terms of components measured in mean-wind coordinates (Fig. 8), denoting these with a tilde:

$$u_1 = \hat{u}_1 \sin\gamma + \hat{u}_2 \cos\gamma, \quad (23)$$

$$u_2 = -\hat{u}_1 \cos\gamma + \hat{u}_2 \sin\gamma. \quad (24)$$

Thus, we have

$$\mathrm{Co}_{12} = \cos\gamma \sin\gamma(\hat{\phi}_2 - \hat{\phi}_1) + \hat{\mathrm{Co}}_{12}(\sin^2\gamma - \cos^2\gamma). \quad (25)$$

Consider first $\hat{\mathrm{Co}}_{12}$, the cospectrum of $\hat{u}_1$ and $\hat{u}_2$. In an idealized (i.e., horizontally homogeneous, barotropic, quasi-steady) boundary layer, $\hat{\mathrm{Co}}_{12}$ (and its integral, $\overline{\hat{u}_1\hat{u}_2}$) differs from zero only due to Coriolis effects. Considering these effects in the context of the Reynolds equation for $\overline{\hat{u}_1\hat{u}_2}$ (Wyngaard, 1982) suggests that $\overline{\hat{u}_1\hat{u}_2}$ should be negative (in the Northern Hemisphere). Model calculations (e.g., Wyngaard *et al.*, 1974) confirm this but also suggest that it is small in the sense that its correlation coefficient $r = \overline{\hat{u}_1\hat{u}_2}/(\overline{\hat{u}_1^2}\,\overline{\hat{u}_2^2})^{1/2}$ does not exceed about 0.2 in magnitude. The AMTEX observations (Lenschow *et al.*, 1980) show that r is very small in the convective PBL, averaging about 0.01 in magnitude. Hence, we will take r to be zero and therefore assume that the second term on the right side of (25) vanishes.

The first term on the right side of (25) involves the difference between $\hat{\phi}_2$ and $\hat{\phi}_1$. According to Panofsky and Dutton (1984), their integrals, $\overline{\hat{u}_2^2}$ and $\overline{\hat{u}_1^2}$, are equal under convective conditions and $\overline{\hat{u}_2^2}$ is about 20% smaller than $\overline{\hat{u}_1^2}$ under neutral conditions. Thus, the contribution of the first term in (25) is also small, and we will take Co_{12} to be zero.

We have evaluated (21) and (22) for typical parameter ranges, assuming $\mathrm{Co}_{12} = 0$, and present the results in Fig. 9. We used $2\alpha = 90$ and 120 degrees, and used $C = 0.95$, 0.85, and 0.75, corresponding (Fig. 7) to $L/d =$ of about 60, 20, and 10, respectively. We evaluated the crosstalk terms by arbitrarily assuming that the u_1 and u_2 spectra were equal, which is not critical

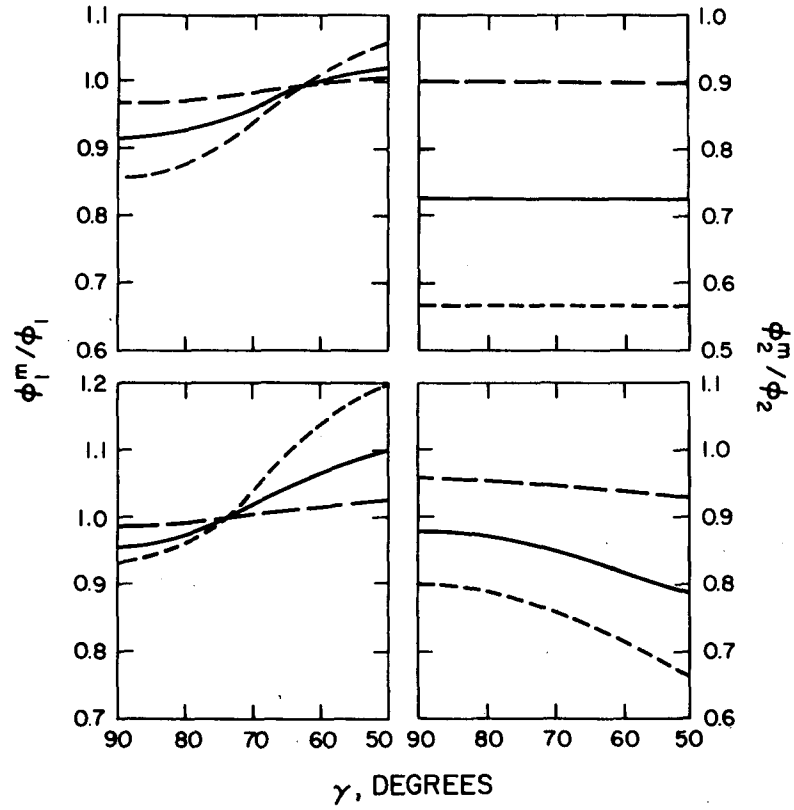

FIG. 9. Calculated spectral response, in anemometer coordinates, for BAO-type transducers. Long-dash: $L/d = 60$; solid: $L/d = 20$; short-dash: $L/d = 10$. Top panel, 90° array; bottom, 120° array.

to the results since the crosstalk terms in (21) and (22) are at most only a few percent of the leading terms.

2) HORIZONTAL VELOCITY SPECTRA IN MEAN-WIND COORDINATES

Turbulent velocities are more often referred to coordinates aligned with the mean-wind vector. We can easily rewrite our results (14) and (15) in these coordinates by rotating our axes through an angle $90° - \gamma$ (Fig. 8), where γ is the mean-wind direction. The result is

$$\hat{u_1}^m = p_1\hat{u_1} + p_2\hat{u_2}, \tag{26}$$

$$\hat{u_2}^m = q_1\hat{u_1} + q_2\hat{u_2}, \tag{27}$$

where we use the carat to denote quantities measured in mean-wind coordinates. The p, q coefficients are

$$p_1 = c_1 \sin^2\gamma - (c_2 + d_1)\sin\gamma\cos\gamma + d_2\cos^2\gamma, \tag{28}$$

$$p_2 = c_2 \sin^2\gamma + (c_1 - d_2)\sin\gamma\cos\gamma - d_1\cos^2\gamma, \tag{29}$$

$$q_1 = -c_2 \cos^2\gamma + (c_1 - d_2)\sin\gamma\cos\gamma + d_1\sin^2\gamma, \tag{30}$$

$$q_2 = c_1 \cos^2\gamma + (c_2 + d_1)\sin\gamma\cos\gamma + d_2\sin^2\gamma, \tag{31}$$

and the c, d coefficients are defined in (16)–(19). The spectral equations are (taking $\hat{\mathrm{Co}}_{12} = 0$)

$$\hat{\Phi}_1{}^m = p_1{}^2\hat{\Phi}_1 + p_2{}^2\hat{\Phi}_2, \tag{32}$$

$$\hat{\Phi}_2{}^m = q_1{}^2\hat{\Phi}_1 + q_2{}^2\hat{\Phi}_2. \tag{33}$$

We evaluated the spectral equations (32) and (33) for the same parameter values used earlier and present the results in Fig. 10. We again evaluated the crosstalk terms by assuming the streamwise and lateral velocity spectra are equal. As before, however, crosstalk has minor influence on the results.

3) THE VERTICAL VELOCITY SPECTRUM

If we start from Eq. (12) for the vertical velocity response, express $\sin\theta$ in terms of the velocity components, and then let the velocity field have mean and fluctuating parts, we obtain an equation for the measured vertical velocity. We find that the error terms in this equation are third order in the fluctuating velocity field, however, so that they are negligible in the linear approximation we are using here. Thus, we can take

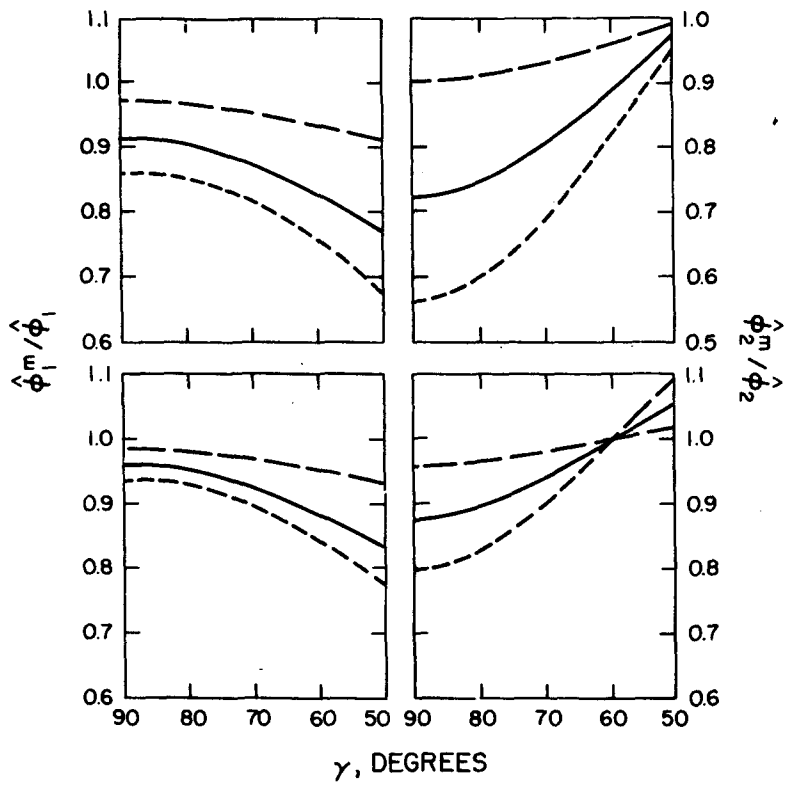

FIG. 10. Calculated spectral response, in mean-wind coordinates, for BAO-type transducers. Curves as in Fig. 9. Top panel, 90° array; bottom, 120° array.

the measured vertical velocity spectrum to be error-free.

4) STRESS COSPECTRA

We can briefly illustrate the transducer-shadow effects on stress. We adopt mean-wind coordinates and denote the cospectra of the horizontal stress components $\overline{\hat{u}_1\hat{u}_3}$ and $\overline{\hat{u}_2\hat{u}_3}$ by $\hat{C}o_{13}$ and $\hat{C}o_{23}$, respectively. Since the u_3 component is unaffected, we have immediately from (26) and (27)

$$\hat{C}o_{13}{}^m = p_1\hat{C}o_{13} + p_2\hat{C}o_{23}, \tag{34}$$

$$\hat{C}o_{23}{}^m = q_1\hat{C}o_{13} + q_2\hat{C}o_{23}. \tag{35}$$

Thus, the measured stress cospectra also suffer attenuation and crosstalk.

The lateral stress $\overline{\hat{u}_2\hat{u}_3}$, while negligible in the surface layer, can be large in mid-PBL. Unfortunately, however, $\overline{\hat{u}_2\hat{u}_3}$ appears to bear no simple relation to $\overline{\hat{u}_1\hat{u}_3}$, so that we cannot make any general statements about the behavior of (34) and (35). Instead, we simply show in Table 1 the values of the p, q coefficients for 90° and 120° arrays with BAO-type transducers for $L/d = 10$ and 20.

With no wake effects, $p_1 = q_2 = 1.0$, $p_2 = q_1 = 0$; we see from Table 1 that the wake effect can cause significant departures from these values. In the surface layer, where the lateral stress $\overline{\hat{u}_2\hat{u}_3}$ is normally negligible, under worst-case conditions ($L/d = 10$, 90° array) $\overline{\hat{u}_1\hat{u}_3}$ can be underestimated by about 20%.

b. Kaijo–Denki-type transducers

The analysis framework of the previous section carries over for Kaijo–Kenki-type transducers, but the crosstalk and attenuation coefficients change. We will briefly discuss the nature of the spectral response this produces.

The spectral response equations (21) and (22) now have coefficients

$$c_1 = f_+ + S_+ \sin\gamma\cos\gamma - S_- \tan\alpha\cos^2\gamma, \tag{36}$$

$$c_2 = f_- \tan\alpha + S_+ \sin^2\gamma - S_- \cos\gamma\sin\gamma\tan\alpha, \tag{37}$$

$$d_1 = f_- \cot\alpha - S_+ \cos^2\gamma + S_- \cos\gamma\sin\gamma\cot\alpha, \tag{38}$$

$$d_2 = f_+ - \cos\gamma\sin\gamma S_+ + S_- \sin^2\gamma\cot\alpha, \tag{39}$$

where

$$f_+ = (f_A + f_B)/2, \tag{40}$$

$$f_- = (f_B - f_A)/2, \tag{41}$$

$$S_+ = \left(\frac{\partial f_A}{\partial\theta_A} + \frac{\partial f_B}{\partial\theta_B}\right)\Big/ 2, \tag{42}$$

TABLE 1. Array response with BAO-type transducers.

γ (°)	$C = 0.75$ ($L/d = 10$)				$C = 0.85$ ($L/d = 20$)			
	p_1	p_2	q_1	q_2	p_1	p_2	q_1	q_2
				90° array				
90	0.93	0*	0*	0.75	0.96	0*	0*	0.85
80	0.91	0.12	0.029	0.77	0.95	0.071	0.017	0.86
70	0.88	0.21	0.046	0.83	0.93	0.13	0.028	0.90
60	0.83	0.27	0.044	0.90	0.90	0.16	0.027	0.94
50	0.77	0.27	0.020	0.97	0.86	0.16	0.012	0.98
				120° array				
90	0.97	0*	0*	0.89	0.98	0*	0*	0.94
80	0.95	0.12	0.011	0.91	0.97	0.073	0.0066	0.95
70	0.92	0.22	0.013	0.95	0.95	0.13	0.0079	0.97
60	0.87	0.29	0*	1.00	0.92	0.17	0*	1.00
50	0.82	0.31	−0.030	1.04	0.89	0.19	−0.018	1.03

* Less than 10^{-3}.

$$S_- = \left(\frac{\partial f_B}{\partial \theta_B} - \frac{\partial f_A}{\partial \theta_A}\right)\Big/ 2. \tag{43}$$

We did calculations for an array with $L/d = 20$, using our shadow-effect parameterization (1b) with $C = 0.83$ and $a = 15.5$, which gives an excellent fit to the Hanafusa *et al.* test data.

For brevity we show in Fig. 11 only the results for the mean-wind coordinates. Note that the response is quite different from that for the same array fitted with

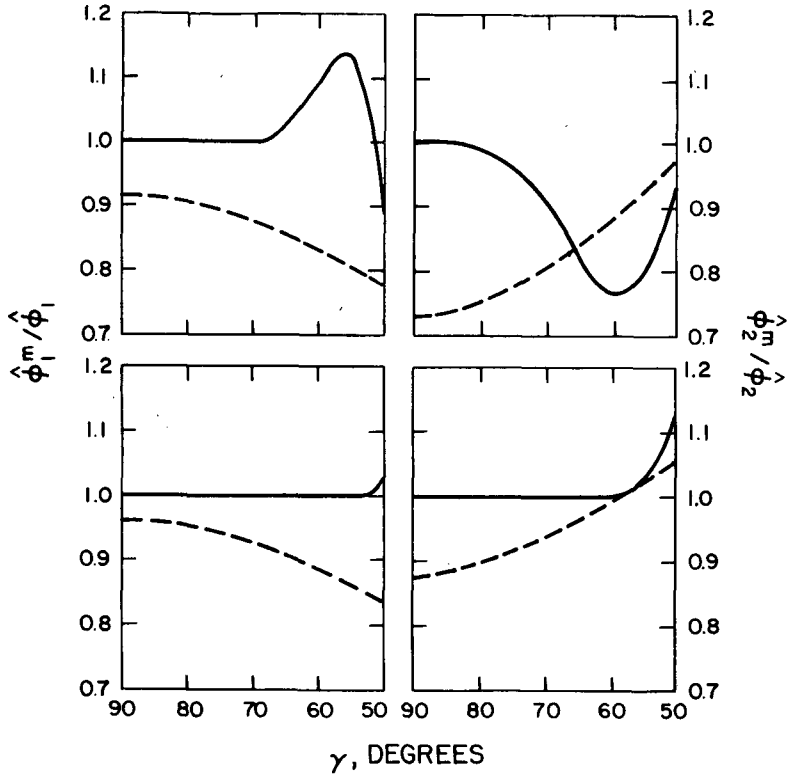

FIG. 11. Calculated spectral response, in mean-wind coordinates, for Kaijo–Denki-type (solid) and BAO-type (dashed) transducers, $L/d = 20$. Top panel, 90° array; bottom, 120°.

BAO-type transducers. The absence of significant wake effects for inclination angles greater than about 30° with Kaijo–Denki transducers (Fig. 6) gives essentially perfect response for wind directions near the axis of symmetry of the array. It is difficult to interpret the details of the response in a simple way, however, because of the complex interactions of the wake effects, the array geometry, the crosstalk and attenuation, and the coordinate rotation. We simply note that the streamwise and lateral responses are quite different in general, and in practice (with high turbulence levels) are probably not as peaked as indicated by our linearized calculations in Fig. 11.

The stress response is again given by (34) and (35). Table 2 shows the p, q coefficients for Kaijo–Denki-type transducers with $L/d = 20$ (i.e., $C = 0.83$ and $a = 15.5$). Note by comparison with Table 1 that the stress response is generally improved over that for BAO-type transducers. Note that for extreme flow angles, however, there can be considerable stress crosstalk.

4. Discussion

The shadow-induced errors indicated by our illustrative results in Figs. 9–11, and Tables 1 and 2, could be detrimental in research applications. For example, researchers often use the appearance of a 4/3 ratio between spectra of lateral (u_2 or u_3) and longitudinal (u_1) velocity components in the inertial subrange as an indicator of local isotropy. Figure 10 shows, however, that for the typical 120° array with $L/d = 20$ and BAO-type transducers uncorrected for wake effects, the u_1 spectrum is attenuated by a factor ranging from 0.96 to 0.83 as the wind direction varies from 90° to 50°, while the u_2 spectrum is modified by a factor ranging from 0.87 to 1.05. The u_3 spectrum is unaffected, to our level of approximation. Hence, the measured ratio of uncorrected u_2 and u_1 spectra in a locally isotropic field would vary from about 1.2 to 1.7, while the measured u_3 and u_1 spectra would have a ratio varying from 1.4 to 1.6. Figure 10 shows that the effects are even stronger in a 90° array.

TABLE 2. Array response with Kaijo–Denki-type transducers.

γ (°)	$C = 0.83$ ($L/d = 20$)			
	p_1	p_2	q_1	q_2
	90° array			
90	1.00	0*	0*	1.00
80	1.00	0.011	0*	0.99
70	0.99	0.11	0.0041	0.95
60	0.94	0.45	0.015	0.88
50	0.85	0.42	0.013	0.96
	120° array			
90	1.00	0*	0*	1.00
80	1.00	0*	0*	1.00
70	1.00	0.0039	0*	1.00
60	1.00	0.049	0*	1.00
50	0.97	0.31	−0.005	1.054

* Less than 10^{-3}.

Mestayer (1982) has critically surveyed the evidence for the 4/3 ratio between u_3 and u_1 spectra in the surface layer. His review indicates that the situation is not yet clear; some researchers (e.g., Kaimal *et al.*, 1972) report finding the 4/3 ratio from sonic anemometer measurements, while others (e.g., Busch, 1973) using hot wires report its onset at frequencies well beyond the range of the sonic anemometer. This situation is complicated by the response problems of hot-wire anemometers which, while having excellent spatial and temporal resolution, suffer from parasitic sensitivities not yet completely understood in atmospheric applications. Mestayer concludes that there are serious doubts about the validity of the 4/3 ratios obtained with sonic anemometers, however, and suggests that they could suffer from response problems due to the transducer wakes.

Our results indicate that the fidelity of measured 4/3 ratios depends very much on L/d, the transducer type, and the alignment of the array with respect to the wind. The Kansas results (e.g., Kaimal *et al.*, 1972) were obtained with Kaijo–Denki transducers in $L/d = 20$ arrays frequently realigned with the changing mean wind direction (J. C. Kaimal, personal communication, 1984), and Fig. 11 indicates their response was satisfactory. On the other hand, Fig. 10 shows that arrays with uncorrected, BAO-type transducers could give unreliable spectral ratios.

As another example, researchers often use the inertial subrange spectral level to infer the dissipation rate of turbulent kinetic energy, using the Kolmogorov expression:

$$\Phi_i = \alpha \epsilon^{2/3} \kappa^{-5/3}, \quad i = 1, 2, \text{ or } 3. \tag{44}$$

Here α is a constant, κ is wavenumber, and ϵ is the dissipation rate. Since from (44) ϵ is proportional to the 1.5 power of inertial range spectral level, it follows that the spectral errors in Figs. 9 and 10 cause correspondingly larger errors in dissipation rate. In the worst case (dissipation found from the u_2 spectrum, using a 90° array with $L/d = 10$ and uncorrected, BAO-type transducers) the dissipation rate is underestimated by nearly 60%. On the other hand, dissipation inferred from the u_3 spectrum would be error free.

If transducer technology permits, minimizing their shadow effects through optimum design seems preferable to compensating for the effects in the subsequent data analysis because the inevitable uncertainties in the shadow data, and the influence of turbulence on the transducer wakes, render these corrections somewhat uncertain. It is possible, for example, that the axial velocity attenuation characteristics of a given array are somewhat different in the turbulent atmosphere and in low-turbulence wind tunnels.

Finally, we emphasize that data from any sonic anemometer are subject to the combined effects of the transducer wakes and the flow distortion caused by the bulk of the array itself. This "probe-induced" flow distortion can be particularly detrimental to stress measurements (Wyngaard, 1981b) but has yet to be studied in detail for sonic anemometers; however, there are disturbing indications (e.g., Kondo and Sato, 1982) that it can be substantial. Until these flow distortion effects are studied, it will be difficult to confirm the transducer-shadow effect experimentally. Nonetheless, in view of our results, we believe it merits the attention of manufacturers and users of sonic anemometry.

Acknowledgments. The senior author is grateful to J. C. Kaimal for numerous helpful discussions on sonic anemometry and for providing material for this paper; to J. A. Businger and C. A. Friehe for suggestions and comments; to B. Stankov for compiling AMTEX data on $\hat{u}_1\hat{u}_2$; to P. Coppin for providing data on the response of his field and commercial model; and to Hope Hamilton and Jo Ann Fankhauser for skillfully producing the manuscript.

REFERENCES

Busch, N. E., 1973: The surface boundary layer. *Bound. Layer Meteor.*, **4,** 213–240.

Coppin, P. A., and K. J. Taylor, 1983: A three-component sonic anemometer/thermometer system for general micrometeorological research. *Bound. Layer Meteor.*, **27,** 27–42.

Friehe, C. A., 1976: Effects of sound-speed fluctuations on sonic anemometer measurements. *J. Appl. Meteor.*, **15,** 434–437.

Hanafusa, T., T. Fujitani, Y. Kobori and Y. Mitsuta, 1982: A new type sonic anemometer-thermometer for field operation. *Pap. Meteor. Geophys.*, **33,** 1–19.

Horst, T. W., 1973: Spectral transfer functions for a three component sonic anemometer. *J. Appl. Meteor.*, **12,** 1072–1075.

Kaimal, J. C., 1979: Sonic anemometer measurement of atmospheric turbulence. *Proc. Dynamic Flow Conference,* Skovlunde, Denmark, DISA Electronic A/S, 551–565.

——, and D. A. Haugen, 1969: Some errors in the measurement of Reynolds stress. *J. Appl. Meteor.*, **8,** 460–462.

——, and J. E. Gaynor, 1983: The Boulder Atmospheric Observatory. *J. Appl. Meteor.*, **22,** 863–880.

——, J. C. Wyngaard and D. A. Haugen, 1968: Deriving power spectra from a three-component sonic anemometer. *J. Appl. Meteor.*, **7,** 827–837.

——, ——, Y. Izumi and O. R. Coté, 1972: Spectral characteristics of surface-layer turbulence. *Quart. J. Roy. Meteor. Soc.*, **98,** 563–589.

——, ——, D. A. Haugen, O. R. Coté, Y. Izumi, S. J. Caughey and C. J. Readings, 1976: Turbulence structure in the convective boundary layer. *J. Atmos. Sci.*, **33,** 2152–2169.

Kondo, J., and T. Sato, 1982: The determination of the von Karman constant. *J. Meteor. Soc. Japan,* **60,** 461–471.

Lenschow, D. H., J. C. Wyngaard and W. T. Pennell, 1980: Mean-field and second-moment budgets in a baroclinic, convective boundary layer. *J. Atmos. Sci.*, **37,** 1313–1326.

Mestayer, P., 1982: Local isotropy and anisotropy in a turbulent boundary layer. *J. Fluid Mech.*, **125,** 475–503.

Mitsuta, Y., 1974: Sonic anemometer-thermometer for atmospheric turbulence measurements. *Flow, its Measurement and Control in Science and Industry,* R. Dowdell, Ed., Instrument Society of America, 341–347.

Panofsky, H. A., and J. A. Dutton, 1984: *Atmospheric Turbulence.* Wiley-Interscience, 397 pp.

Wyngaard, J. C., 1981a: Cup, propeller, vane, and sonic anemometers in turbulence research. *Annual Review of Fluid Mechanics* Vol. 13, Annual Reviews, 399–423.

——, 1981b: The effects of probe-induced flow distortion on atmospheric turbulence measurements. *J. Appl. Meteor.*, **20,** 784–794.

——, 1982: Boundary-layer modeling. *Atmospheric Turbulence and Air Pollution Modelling,* F. T. M. Neuwstadt and H. Van Dop, Eds., Reidel, 358 pp.

——, O. R. Coté and K. S. Rao, 1974: Modeling the atmospheric boundary layer. *Advances in Geophysics,* Vol. 18A, Academic Press, 193–211.